PCCP

Atomic-scale Structure of Misfit Dislocations in CeO2/MgO Heterostructure and Thermodynamic Stability of Dopant-defect Complexes at the Heterointerface

Journal:	*Physical Chemistry Chemical Physics*
Manuscript ID	CP-ART-07-2019-003727.R1
Article Type:	Paper
Date Submitted by the Author:	08-Aug-2019
Complete List of Authors:	Dholabhai, Pratik; Rochester Institute of Technology, School of Physics and Astronomy

Atomic-scale Structure of Misfit Dislocations in CeO_2/MgO Heterostructure and Thermodynamic Stability of Dopant-defect Complexes at the Heterointerface

Pratik P. Dholabhai*

School of Physics and Astronomy
Rochester Institute of Technology
Rochester, NY 14623

* Email: pratik.dholabhai@rit.edu

Abstract

Complex oxide heterostructures and thin films have found applications across the board in some of the most advanced technologies, wherein the interfaces between the two mismatched oxides influence novel functionalities. It is imperative to comprehend the atomic-scale structure of misfit dislocations, which are ubiquitous in semi-coherent oxide heterostructures, and obtain a fundamental understanding of their interaction with point defects and dopants to predict and control their interface-governed properties. Here, we report atomistic simulations elucidating the atomic-scale structure of misfit dislocations in CeO_2/MgO heterostructure. Our results demonstrate that the 45º rotation of CeO_2 thin film is one of the potential fundamental mechanisms responsible for eliminating the surface dipole, leading to the experimentally observed mixed epitaxial relationship. We further report the thermodynamic stability of diverse dopant-defect complexes near misfit dislocations, wherein various scenarios for nearest neighbor bonding environments within the complexes are explored. Complex misfit dislocation structure, asymmetry, strain, and the availability of diverse nearest neighbor bonding environment between dopants and oxygen defects at the interface are accountable for a wide dispersion in energies within a given dopant-defect arrangement. As opposed to the bulk, the thermodynamic stability of oxygen vacancy is found to be sensitive to the dopant arrangement at the heterointerface. Extended stabilities of dopant–defect complexes at misfit dislocations reveal that they would influence ionic transport at heterointerfaces of fluorite-structured thin film electrolytes. Notably, results herein offer a fundamental atomic-scale perspective of the intricate interplay between dopants, defects, and misfit dislocations at the heterointerfaces in mismatched oxide heterostructures.

Keywords: thin film oxide electrolytes, solid oxide fuel cells, doped ceria, misfit dislocations, ionic conductivity

1. Introduction

Complex oxide heterostructures,[1,2,3] an intriguing class of materials fabricated by marrying two dissimilar oxides have mesmerized the scientific community as they exhibit superior and emergent properties than their individual constituents.[4,5,6] In complex oxide heterostructures, the interfaces between the two dissimilar oxides are critical as they offer diverse modes to introduce non-homogeneity in the material. This non-homogeneity is often manifested in substantial enhancement of material properties for applications in Solid Oxide Fuel Cells (SOFCs),[7,8,9] batteries,[10] nuclear materials,[11] catalysis,[12] solar cells,[13] information storage,[6,14] *etc*. Consequently, selective mixing of oxides in a highly tailored morphology with large volume fraction of interfacial area is a widespread approach to design oxide heterostructures with enhanced functionalities. However, the basic role of interfaces and their intricate interaction with wide variety of defects, which are pervasive at such interfaces, is not well understood.

A coherent interface is formed in oxide heterostructures with small mismatches and the lattice mismatch is completely compensated by elastic strain. In semi-coherent oxide heterostructures, when an epitaxial layer is grown on the substrate above the critical thickness of the film, misfit dislocations are formed to alleviate the coherency strain between the two materials with different lattice constants. Essentially, in semi-coherent oxide heterostructures, misfit dislocations are the inevitable microstructural feature present at the heterointerface between the two mismatched oxides.[15] High interface to volume ratio in nanostructured thin films lead to high density of misfit dislocations at the interface. As a result, the role of misfit dislocations in semi-coherent oxide heterostructures have been investigated for applications pertinent to fast ion conduction, [16,17,18,19,20,21,22,23,24,25] enhanced radiation damage, [26,27,28,29] ferroelectrics,[30,31] transparent conducting semiconductors,[32] catalysis,[33] *etc*. Nonetheless, the influence of strain and misfit dislocations on properties pertinent to energy applications is not well understood.[34,35]

Widespread deployment of SOFC technology necessitate lowering their operating temperatures to intermediate-temperature (IT-SOFC) range of 773–973 K.[36,37,38,39,40,41] One promising route toward achieving this goal is via implementation electrolytes based on oxide thin films and heterostructures,[7,8,9,16,17,18,19,20,21,22,23,24] which exhibit superior performance at lower temperatures and are poised to take over as next-generation IT-SOFC electrolytes.[36,38] However, atomistic mechanisms responsible for the experimentally

observed fast ionic conduction across oxide interfaces, specifically at misfit dislocations, are not well understood. This ambiguity exists due to the polarized results in the community, wherein some experiments hypothesize misfit dislocations as pathways for fast ionic transport,[7,8,9,16,17,18,19,20,21,22] whereas the others do not observe this enhancement.[23,24,42,43] In addition, few computational studies report that homophase dislocations [44,45] and misfit dislocations [25] hamper oxide ion conductivity.

Doping is characteristically used as an effective strategy to alter, and in some cases control the properties of oxides. Fluorite-structured (CaF_2) doped ceria (CeO_2) is an extrinsic ionic conductor widely used as bulk electrolyte in SOFCs.[38,46,47,48,49,50,51,52,53,54] In solid oxide electrolytes based on doped ceria, trivalent dopants replacing tetravalent sites have a net effective charge that affects the electroneutrality condition and the defect equilibria, which lead to the formation of oxygen vacancies. Enhanced vacancy concentrations due to the addition of aliovalent dopants is primarily responsible for higher ionic conductivity in doped ceria, which is sensitive to the dopant type and concentration.[46,47,48,55,56,57,58,59,60,61,62,63,64,65] The complex interplay between trivalent dopants and oxygen vacancies is well understood in the bulk, where it has been shown that the migration enthalpy is minimized in the vicinity of dopants.[46,47,48,57,58,62] Moreover, fundamental mechanisms for the optimal performance of bulk doped ceria-based oxide electrolytes are well documented.[56,62,64,65] Nonetheless, the same cannot be argued for the case of semi-coherent oxide heterostructures assembled using doped ceria-based thin films.

In oxide heterostructures, possible features that are altered at the interfaces as compared to the bulk are chemical composition and stoichiometry,[66] which depend on the processing conditions as well as the atomic-layer chemistry of the two dissimilar oxides that are married. Consequently, a vast spectrum of complex interface structures is probable in oxide heterostructures. If we add to this mix the existence of dopants,[67,68,69,70] point defects,[71,72,73,74] and structural defects,[28,29] what we encounter is a multifaceted interplay between point defects, dopants, and extended defects (misfit dislocations). In bulk electrolytes based on doped ceria, at low temperatures, dopants and oxygen vacancies form stable complexes that influence oxide ion conductivity. This is also true for dopant-defects complexes near grain boundaries in nanocrystalline doped ceria.[75] Vitally, as oxygen vacancies in doped ceria can exist at first, second or third nearest neighbor positions relative to the dopant ion, [56,57,63,65,76] the fundamental structure of dopant-defect

clusters at misfit dislocations will unequivocally influence ionic conductivity. As compared to the bulk, the dopant-defect cluster is also expected to vary at the interface due to modifications in atomic structure and local strain. Finally, as observed in bulk doped ceria,[56,57,63,65] different dopant species are expected to prefer distinct dopant-defect structures at misfit dislocations. However, in oxide heterostructures, especially at misfit dislocations, the role of dopant-defect complexes is not well understood. From a fundamental perspective, while dopants segregation at misfit dislocations is not well understood, it is anticipated to impact interface-governed properties. For instance, we have recently established that oxygen vacancy segregation [25,26] and dopant segregation [67] behavior in oxide heterostructures is influenced by the atomic-layer chemistry and structure of misfit dislocations, underpinning the importance of understanding the fundamental interaction of oxygen vacancies and dopants with misfit dislocations. As trivalent dopants in ceria lead to oxygen vacancies (defects), gauging the stability of dopant-defect complexes at misfit dislocations will be imperative to understand the fundamental mechanisms for ionic conduction and evaluate the performance of thin film electrolytes based on doped ceria.

Due to the popularity of doped ceria as oxide ion conductors, oxide heterostructures synthesized by utilizing ceria and doped ceria thin films deposited on MgO substrates have been extensively studied.[77,78,79,80,81,82] Lattice constants of CeO_2 and MgO are vastly different with a mismatch of roughly 28.4%. Experimentally, for cube-on-cube epitaxy, the large lattice mismatch between doped ceria and MgO result in an almost continuous line of misfit dislocations that mitigate the stress at the interface.[77,79,81] Conversely, there are studies that have not reported the presence of misfit dislocations at the CeO_2/MgO interface, although the strain relieving mechanisms in such cases are not clear.[78,80,82] It has been shown that there are two competing in-plane orientations for CeO_2/MgO interface, $[100]_{CeO2}||[100]_{MgO}||Interface$ and $[110]_{CeO2}||[100]_{MgO}||Interface$, wherein the latter has lower interfacial energy.[78,80] Furthermore, when CeO_2 is rotated around the surface normal by 45°,[78,79] the epitaxial misfit decreases to ~9.1% for the $[110]_{CeO2}||[100]_{MgO}||Interface$ orientation relationship. Irrespective of the epitaxial relationship, it is evident that the mismatch at the CeO_2/MgO interface is quite large, indicating that misfit dislocations would be present at the interfaces to relieve the large coherency strain in these semi-coherent heterostructures.[77,79,81]

Although the significance of misfit dislocations in semi-coherent CeO_2/MgO heterostructures is unambiguous, their atomic-scale structure and stability is not well understood. From an experimental standpoint, basic information pertaining to the atomic-scale structure of individual column of atoms in the neighborhood of misfit dislocations is not easily accessible due to buried interfaces and metastable heterostructures encountered during synthesis. Even from a computational perspective, as summarized in our recent review article,[83] the key challenge in mimicking misfit dislocations in semi-coherent oxide heterostructures is to employ very large supercells so as to include the fully relaxed thin films deposited on mismatched substrates.[26] Density functional theory (DFT) based studies, [84,85,86,87] focused on either coherent or artificially strained interfaces in order to decrease the supercell size and the computational cost, are unable to embrace the true atomic-scale structure of semi-coherent heterostructures.[83] As a result, atomistic simulations based on empirical potentials has often been the method of choice to interpret the fundamental atomic-scale structure of misfit dislocations. Once a stable structure has been identified, further studies that predict the structure and stability of dopant-defect complexes at misfit dislocations can be achieved, which will ultimately offer basic insights into the influence of these complexes on ionic transport.

Here, we report results based on atomistic simulations to predict the atomic-scale structure of misfit dislocations in model CeO_2/MgO heterostructure, which elucidates the experimentally observed mixed epitaxial relationship. We further examine the structure and stability of a wide range of dopant-defect clusters in the neighborhood of misfit dislocations. Complex misfit dislocation structure, asymmetry, strain, and the availability of diverse nearest neighbor bonding environments between dopants and oxygen defects at the interface are responsible for a wide dispersion in energies of a given dopant-defect complex arrangement. Notably, results herein shed light on the importance of understanding the basic dopant-defect interactions at misfit dislocations, which influence the ionic transport in thin film oxide electrolytes based on oxide heterostructures.

2. Methodology

2.1. Computational framework

Atomistic simulations with 3D periodic boundary conditions (PBC) were conducted within the framework of Large-scale Atomic/Molecular Massively Parallel Simulator

(LAMMPS).[88] The simulations are based on energy minimization using a classical Born-like description of an ionic solid. Parameterized Buckingham[89] pair potentials are utilized to describe the two-body short-range interactions, whereas interactions due to the long-range Coulombic (electrostatic) forces were calculated by means of Ewald's method.[90] Parameters for the Buckingham pair potential as derived by Busker *et al*. were used for MgO.[91] Pair potentials derived by Minervini *et al*.[92] and Zacate *et al*.[93] were employed for CeO_2 and Y^{3+}, Gd^{3+}, Sm^{3+}, and La^{3+}, respectively. These interatomic potential parameters were chosen as all the cation interactions (divalent, trivalent, and tetravalent) were fitted against the same O^{2-} – O^{2-} potential. Large-scale simulations were performed using Extreme Science and Engineering Discovery Environment (XSEDE) resources.[94]

2.2 Formation of dopant-defect clusters

Enhanced oxide ion conductivity in doped ceria is primarily achieved due to higher vacancy concentration resulting from the charge balance after the incorporation of aliovalent dopants. The defect reaction that governs the addition of trivalent dopants to ceria can be expressed in Kröger-Vink notation as:

$$M_2O_3 \xrightarrow{CeO_2} 2M'_{Ce} + V_{\ddot{O}} + 3O_O^{\times} \qquad (1)$$

where M and $V_{\ddot{O}}$ correspond to trivalent dopant and oxygen vacancy, respectively. This relationship indicates that the substitution of two tetravalent cerium ions with trivalent dopant ions on the cation sublattice will result in an oxygen vacancy on the anion sublattice. At low temperatures, this will lead to the formation of dopant-defect clusters $\left(V_{\ddot{O}}\, 2M'_{Ce}\right)$, which will be hereafter denoted as M–$V_{\ddot{O}}$–M clusters. Henceforth, the notations 1NN, 2NN, and 3NN will correspond to oxygen vacancies at the first, second, and third nearest neighbor (NN) to the dopant ions, respectively. As described by the defect reaction in Equation 1, after the introduction of trivalent dopants in ceria, oxygen vacancies are formed on the anion sublattice at 1NN, 2NN, or 3NN to the dopant, forming M–$V_{\ddot{O}}$–M clusters.[47,48,56,57,62] These M–$V_{\ddot{O}}$–M clusters are found to have high binding energies resulting from the strong electrostatic and elastic interactions between the negatively charged dopant ions and the positively charged oxygen vacancies. Consequently, there is a reasonable fraction of such complexes in doped ceria, especially at low temperatures. In bulk ceria, the preferred position of oxygen vacancies relative to the dopants and the overall binding of the dopant-

defect complex are found to be dependent on the ionic radius of the dopants. [47,48,56,57,62] Accordingly, ionic conductivity of trivalent-doped ceria is also found to depend on the ionic radius of dopants.[95] Nevertheless, there is a lack of understanding of this fundamental defect reaction and the formation of M–$V_{\ddot{O}}$–M clusters at misfit dislocations in oxide heterostructures deposited using doped ceria thin films. As this basic knowledge can facilitate the design of highly conductive thin film electrolytes, we address this key issue by studying the energetics of various M–$V_{\ddot{O}}$–M clusters (each cluster has two trivalent dopants and an oxygen vacancy) near the misfit dislocations.

Henceforth, the notation *x*NN–*y*NN will correspond to an M–$V_{\ddot{O}}$–M cluster wherein the oxygen vacancy is at *x* (*x* = 1,2,3) NN to dopant 1 and at *y* (*y* = 1,2,3) NN to dopant 2. As an example, 2NN–1NN indicates that the oxygen vacancy is 2NN to dopant 1 and 1NN to dopant 2. For clarity, we will refer to the family of all possible *x*NN–*y*NN clusters for a given *x* and *y* as "arrangements" and specific configurations within a given arrangement as "clusters" or "complexes". In CeO_2 thin film considered in this study, we have examined several structural variants of M–$V_{\ddot{O}}$–M clusters for each *x*NN–*y*NN arrangement in the bulk and at the interface for all dopants. We have not considered interactions beyond 3NN, as the interaction between dopants and oxygen vacancies is anticipated to diminish at large separation. In bulk ceria with lattice parameter *a* = 0.5411 nm,

$$\left.\begin{aligned} d_{(Ce-O)}1NN &= \frac{\sqrt{3}a}{4} = 0.2343 \text{ nm} \\ d_{(Ce-O)}2NN &= \frac{\sqrt{11}a}{4} = 0.4487 \text{ nm} \\ d_{(Ce-O)}3NN &= \frac{\sqrt{19}a}{4} = 0.5897 \text{ nm} \end{aligned}\right\} \quad (2)$$

where, $d_{(Ce-O)}xNN$ is the distance between a cerium ion and oxygen ion that are at *x*NN to each other. Although these distances are approximately fixed in the bulk, they will vary near the misfit dislocations due to strain, asymmetry, open structures, and varied bond lengths, a consequence of the complicated atomic arrangement at the interface. As discussed later, for the minimized CeO_2/MgO heterostructure, we found fluctuations in bond lengths, which are maximum in the vicinity of the interface plane. To incorporate this variation in bond length in our exploration of various *x*NN–*y*NN cluster arrangements at the

interface, we added a cutoff of ± 0.015 nm to define the NN distance. For instance, a bond distance is termed 1NN if it ranges between 0.2193 nm < $d_{(Ce-O)}1NN$ < 0.2493 nm.

We have utilized fully stoichiometric CeO_2/MgO heterostructure model, wherein the supercell size is ~ 4.21 × 3.38 × 8.9 nm^3. The 11,274 atom supercell consists of 1518 Ce atoms, 6396 O atoms, and 3360 Mg atoms. This stoichiometric model was used to study dopants-defects clusters for four trivalent dopants, namely Y^{3+}, Gd^{3+}, Sm^{3+}, and La^{3+}. This allows us to examine the effect of dopant size mismatch and strain at misfit dislocations. For screening the various *x*NN–*y*NN arrangements of the M–$V_{\ddot{O}}$–M clusters at the interface, the two layers considered for their placement are denoted by Layer-1 and Layer-2, wherein Layer-1 is the layer that is directly in contact with MgO, whereas Layer-2 is one atomic-layer further away from the interface (Layer-1). It is possible that the effect of the interface could extend beyond the chosen layers. However, these layers best signify the interface and its immediate proximity, and are expected to essentially capture the influence of misfit dislocations on the M–$V_{\ddot{O}}$–M clusters. Henceforth, for a given M–$V_{\ddot{O}}$–M cluster, its location in Layer-1 will indicate that the oxygen vacancy is precisely in Layer-1, but the dopants could either be in Layer-1, Layer-2 or Layer-3, or a combination of these layers. Analogously, for a cluster in Layer-2, the oxygen vacancy is strictly in Layer-2, but the dopants could reside in the same layer or in the neighboring layers. Not only is this approach imperative to investigate various arrangements of M–$V_{\ddot{O}}$–M clusters in the thin film, but it also demonstrates the inherent structural complexity involved in studying them.

For evaluating the role of M–$V_{\ddot{O}}$–M clusters in doped ceria, after their inclusion, energy minimization was performed wherein the ionic positions were allowed to fully relax prior to computing the energies. Throughout the simulations, the volume was held constant at the supercell volume without the cluster. During the test calculations, we found that the volume relaxation has a rather minor effect on the defect energetics. Importantly, cluster-cluster interactions are not present in the system since clusters are studied one at a time. Within this dilute limit, our assumption of performing calculations at constant volume is justified. Vitally, we have utilized this supposition to successfully investigate segregation at surfaces,[96,97] grain boundaries, [75,98] and heterointerfaces[67] in oxides, and compare with experimental data. Besides, this assumption has also been employed in the literature.[46] In our approach, the cluster energy is essentially computed as the relative change in total energy of the system due to the placement of dopant-defect clusters at different locations.

For a given material, the relative cluster energy is computed as the difference in energy between the dopant-defect cluster at the most favorable location and the respective site. A simplified equation for computing the segregation energy is given by $\boldsymbol{E_{seg}} = \boldsymbol{E^{int}}(\boldsymbol{x}) - \boldsymbol{E^{min}}(\boldsymbol{x})$, where $\boldsymbol{E^{int}}(\boldsymbol{x})$ is the energy of the dopant-defect cluster $\boldsymbol{x}$ at the respective site and $\boldsymbol{E^{min}}(\boldsymbol{x})$ is the energy of dopant-defect cluster $\boldsymbol{x}$ at the most favorable site in a given material. Hence, it is the relative driving force for the dopant-defect complex to reside at a given location as compared to the most favorable site (which, for a given dopant species, is taken as the zero of energy). In this scheme, higher the energy, lower the stability and vice versa. For various trivalent dopants, these energies are plotted as a function of dopant-defect cluster arrangement in Layer-1 and Layer-2. The strategy used in this work has been successfully used in the past to study relative trends in dopant segregation at misfit dislocations,[67] surfaces,[96,97] and grain boundaries[75,98] in oxides, as well as grain boundaries in metals.[99]

3. Results

3.1. Atomic-scale structure of the CeO_2/MgO heterointerface

To predict the atomic-scale structure of the interface, a model CeO_2/MgO heterostructure was constructed using the experimentally observed mixed epitaxial relationship, wherein $[1\bar{1}0]_{CeO2}||[100]_{MgO}||Interface$ and $[001]_{CeO2}||[010]_{MgO}||Interface$, as depicted in (**Figure 1**). Since the lattice parameters are a_{CeO2} = 0.5411 nm and a_{MgO} = 0.4212 nm, the lattice mismatch resulting from the cube-on-cube orientation relationship in CeO_2/MgO heterostructure is very large (~28.4%).[77,78,79,80,81,82] It is important to note that alternating planes of Ce and O atoms in the CeO_2 $[001]$ direction are responsible for the polar nature of the $[001]$ surface. As a result, at the interface, both Ce and O terminated planes are possible for cube-on-cube epitaxial relationship. To eliminate the surface dipole, we have rotated the CeO_2 thin film by 45° around the surface normal so as to achieve the aforementioned orientation relationship, which is observed in experiments. Owing to this approach, strain along the $[1\bar{1}0]$ direction of the thin film is reduced to ~9.1%, whereas that along the $[001]$ direction still remains ~28.4%. Due to this orientation relationship, along the $[1\bar{1}0]$ direction of the thin film, 11 unit cells of $CeO_2[1\bar{1}0]$ have to be matched with 10 unit cells of MgO[100]. On the other hand, along the $[001]$ direction of the thin film, 3 unit cells of $CeO_2[001]$ have to be matched with 4 unit cells of MgO$[010]$. This deposition approach is

necessary to ensure that the bicrystal has minimal extrinsic strain and there is no dipole in the material. From a computational perspective, in addition to mimicking the experimentally observed epitaxial relationship, this strategy ensures that the structural model is stable as there are no charged planes at the interface. Essentially, misfit dislocations are present in the supercell due to this construction scheme, which matches different number of atomic columns across the interface. In accordance with the model construction, along the $[001]$ direction of the thin film, size of the cell is smaller (~1.69 nm) as compared to the $[1\bar{1}0]$ direction, wherein the size of the cell is larger (~4.21 nm). Since this model heterostructure with misfit dislocations will be later utilized to perform calculations for dopant-defect cluster stability, supercell size along the $[001]$ direction of the thin film was doubled to avoid the interaction between clusters in periodic cells. The resulting as-constructed heterostructure has the dimensions of ~ 4.21 × 3.38 × 8.9 nm^3, wherein z-axis corresponds to the supercell thickness, which includes the thickness of the thin film and the substrate. As a consequence of PBC, there are two identical interfaces in the direction of the interface normal (z-axis).

Figure 1. *Minimum energy structure of the CeO_2/MgO heterostructure for the experimentally observed orientation relationship. Within the same supercell, misfit dislocations at the heterointerface are zoomed in as viewed along two different directions (a)* $[110]_{CeO2}||[100]_{MgO}||$Interface *and (b)* $[001]_{CeO2}||[010]_{MgO}||$Interface*. Ce and Mg ions are indicated by yellow and green spheres, respectively. For clarity and contrast,* O_{CeO2} *(blue) and* O_{MgO} *(red) spheres are colored differently.*

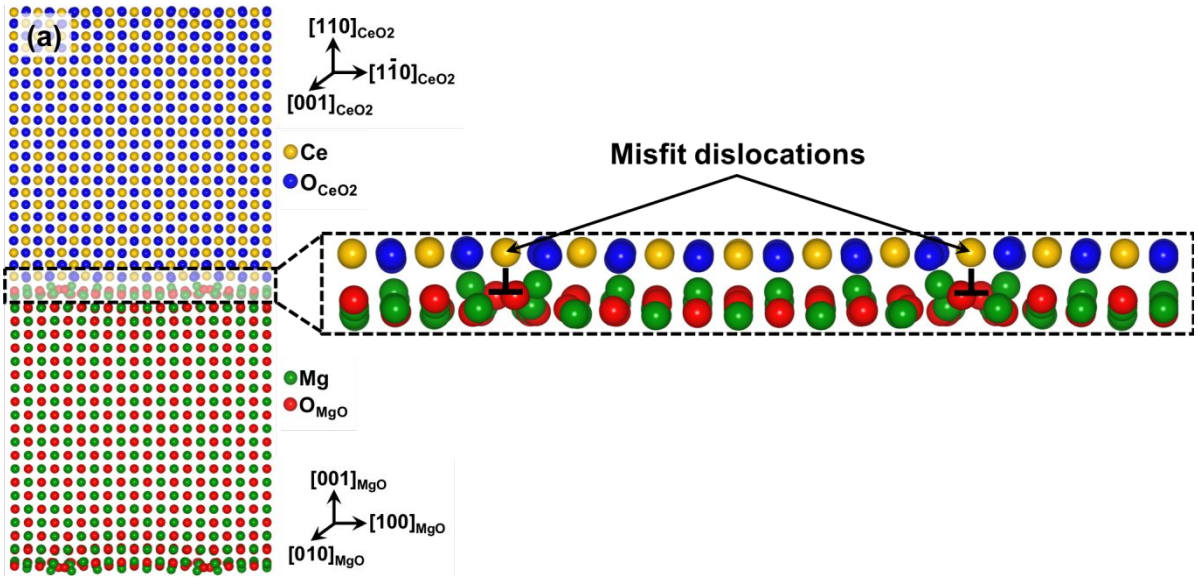

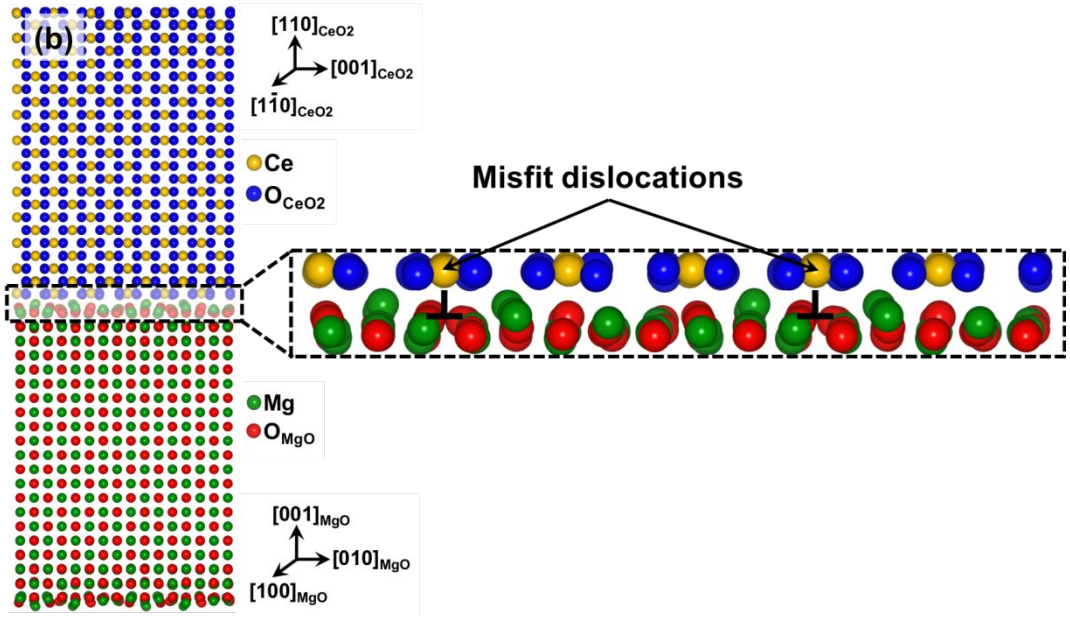

For the minimized heterostructure, **Figures 1(a)** and **1(b)** depict the side view of the stoichiometric supercell, and as a result, misfit dislocation structure along $[1\bar{1}0]$ and $[001]$ directions of CeO_2, respectively. As compared to the as-built model, the supercell parameters changed marginally in the minimized heterostructure. Orientation relationship between the two materials is also shown for clarity. The interface layers are zoomed in to clearly display the extra column of thin film atoms, the so-called misfit dislocations, at the interface as viewed along two different directions. Evidently, the misfit dislocation spacing is different in both directions owing to dissimilar strain. To gain further insights into the precise misfit dislocation structure in the minimized heterostructure, **Figure 2** offers a normal view of the interface layers in CeO_2 and MgO, where only one atomic layer on each side of the interface is shown. In **Figure 2**, the relaxed supercell is extended in the *x* and *y* directions (2 × 2 × 1) for better visualization. This heterostructure was found to be structurally stable after undergoing annealing at 1,000 K for 1 ns, wherein minor reconstructions were observed at the interface, mostly on the MgO side.

Figure 2. *Interface layers of the minimized CeO_2/MgO heterostructure shown in Figure 1. The view is normal (CeO_2 thin film is above MgO substrate in this view) to the interface plane. In this image, the relaxed supercells are extended in the x and y directions* (2 × 2 × 1) *for better visualization. To clearly depict the misfit dislocation structure and spacing, only*

one atomic layer on each side of the interface is shown. The purple and pink boxed regions show misfit dislocation network. Black circles are shown to emphasize periodic regions that lack atoms. Color scheme for ions is shown below the figure, which is same as in Figure 1.

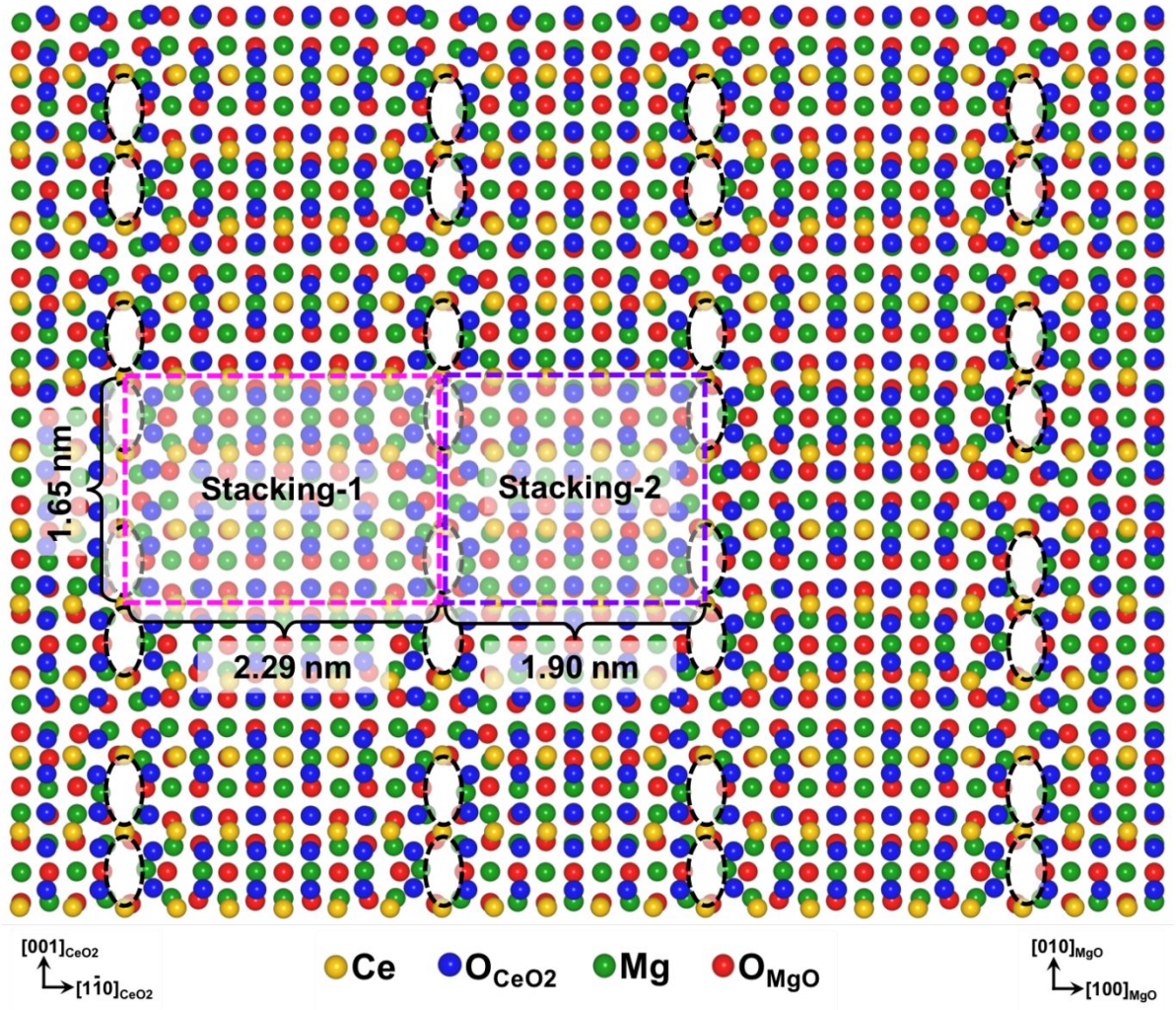

As evident in **Figure 2,** structural relaxation at the interface between the mismatched materials lead to a rather complex atomic arrangement. In some cases, counterions are bonded across the interface, whereas in some instances, repulsive interactions comprising cation-cation and anion-anion bonding is observed across the interface. Periodic regions of open spaces at the interface are emphasized by black circles. Along the CeO_2 $[001]$ direction, a Burgers vector of $a_{<100>}$ is projected for the misfit dislocations, wherein a full dislocation is separated by 1.65 nm (**Figure 2**). Along the CeO_2 $[1\bar{1}0]$ direction, the misfit dislocations are split into partials with a Burgers vector of $\frac{a_{<110>}}{2}$. These partials are

separated by a stacking fault. The most remarkable feature present at the interface (**Figure 2**) is that albeit each partial is repeated after 4.19 nm, they are separated by unequal distances along the CeO_2 $[1\bar{1}0]$ direction, which is a result of the mismatched unit cells at the interface. For instance, in **Figure 2**, Stacking-1 (pink boxed region) has 6 unit cells of $CeO_2[1\bar{1}0]$ matched with 5.5 unit cells of MgO[100], whereas Stacking-2 (purple boxed region) consists of 5 unit cells of $CeO_2[1\bar{1}0]$ matched with 4.5 unit cells of MgO[100] (in total, 11 unit cells of $CeO_2[1\bar{1}0]$ are matched with 10 unit cells of MgO[100]). In order to minimize the strain in the heterostructure, $CeO_2[1\bar{1}0]$ lattice constant is slightly swollen in Stacking-1, whereas it is somewhat reduced in Stacking-2. It is important to note that the multifaceted atomic arrangement uncovered at the CeO_2/MgO interface within the two predominant stackings and the resulting misfit dislocation structure has not been reported in the past. Importantly, these results underpin the vital role of misfit dislocations in mitigating the coherency strain and influencing the atomic-scale structure and stability of semi-coherent heterostructures.

3.2 Stability of dopant-defect clusters in Layer-1 of the CeO_2 thin film

Thermodynamic stabilities in terms of energy ranges for various M–$V_{\ddot{O}}$–M clusters within different *x*NN–*y*NN arrangements encountered in the bulk and in Layer-1 of the thin film are given in **Figure 3**. The nomenclature for various clusters is given in Section 2. As per our definition of clusters, their location in Layer-1 implies that oxygen vacancies are strictly in Layer-1, but the associated dopants could be present in Layer-1, Layer-2 or Layer-3. Henceforth, dopant-defect clusters comprising of Y^{3+}, Gd^{3+}, Sm^{3+}, and La^{3+} will be denoted as clusters in Y-doped ceria (YDC), Gd-doped ceria (GDC), Sm-doped ceria (SDC), and La-doped ceria (LDC), respectively. For all results presented in this work, for a given material system, energies are shifted such that 0 eV corresponds to the most favorable location (maximum stability) for the M–$V_{\ddot{O}}$–M cluster within that material, which could be either in the bulk, Layer-1, or Layer-2. In this scheme, higher the energy of the cluster, lower the stability. To facilitate comparison with stabilities of arrangements within the bulk, for each material system, black bars in **Figure 3** correspond to the respective energies in the bulk for a given arrangement. For a particular cluster arrangement, whilst a single energy value is expected in the bulk, there is slight variation in energies due to the overall strain in the system.

As depicted in **Figure 3**, in YDC, GDC, SDC, and LDC, the 2NN–2NN arrangement within Layer-1 is found to be the most favorable. Nonetheless, it is unlikely that clusters in Layer-1 will exclusively have 2NN–2NN arrangement, since there are other arrangements that are only slightly higher in energy and thus, are likely to coexist. The 3NN–3NN arrangement is found to be the least favorable across all dopants. Interestingly, as opposed to the interface (Layer-1), the most favorable arrangement in the bulk for YDC, GDC, and SDC are 1NN–1NN, 1NN–2NN, and 1NN–2NN, respectively. For LDC, 2NN–2NN arrangement is the most stable at the interface as well as in the bulk. This result reveals that understanding the most stable arrangement for clusters in the bulk of CeO_2 is not sufficient to comprehend their arrangement at the interface of CeO_2/MgO heterostructure. Furthermore, the existence of misfit dislocations at the interface strongly influences the stability of clusters.

Figure 3. *Energy ranges for various M–$V_{\ddot{O}}$–M cluster arrangements in the bulk and at Layer-1 (interface layer) of the CeO_2 thin film in the CeO_2/MgO heterostructure. Here, Ce^{4+} ions are replaced by trivalent dopants Y^{3+}, Gd^{3+}, Sm^{3+}, and La^{3+}. Vertical bars represent the spread in energy (eV) for the various xNN–yNN arrangements indicated by different colors for each trivalent dopant. Energies are scaled so that 0.0 eV indicates the most favorable xNN–yNN arrangement of the M–$V_{\ddot{O}}$–M cluster.*

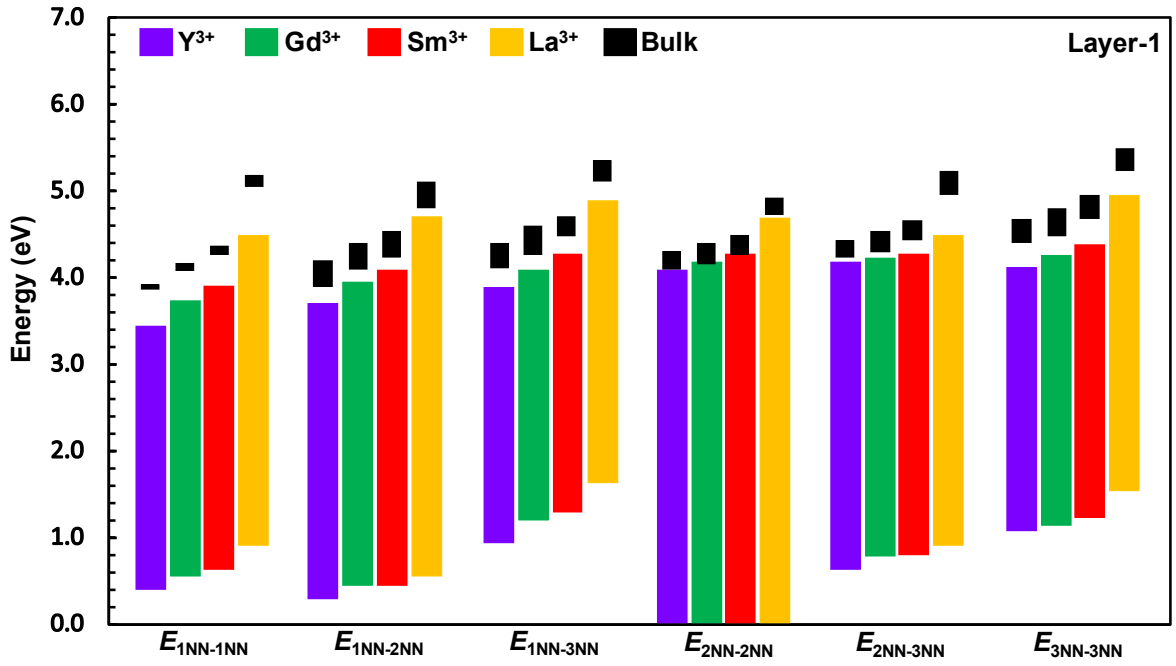

A remarkable feature to note in **Figure 3** is the spread (vertical bars) in energies, which reveal that for a given *x*NN–*y*NN arrangement in YDC, GDC, SDC, and LDC, the stability of various clusters within the same arrangement vary greatly. As anticipated, observed spread in energies is not present in the bulk. To shed light into the observed non-homogeneity in energies, **Figure 4** illustrates few representative M–$V_O^{\cdot\cdot}$–M clusters for 2NN–2NN (most favorable) arrangement in Layer-1. For each of the dopant species, diverse clusters are highlighted in different colors, and their respective energies are given in **Table 1**. Clusters were screened only in one half interface plane as shown in **Figure 4**, since the second half is symmetric due to supercell extension as explained in Section 2. One common trend observed for all the dopants is that the lowest energy M–$V_O^{\cdot\cdot}$–M cluster with 2NN–2NN arrangement shows distinct location preference at the interface, specifically in the vicinity of misfit dislocations. For instance, clusters 1 and 12 are found to be most favorable across all the dopants. In contrast, cluster 2 is one of the least favorable, indicating that not all clusters with 2NN–2NN arrangement will be preferred at the interface.

In order to further examine the spread in energies within other cluster arrangements, **Figure S1** in Supplementary Information illustrates few representative M–$V_O^{\cdot\cdot}$–M clusters for 1NN–2NN (second most favorable) arrangement in Layer-1. In **Figure S1**, for each of the dopant species, dissimilar clusters are highlighted in different colors, and their respective energies are given in **Table S1**. Comparable to the trend observed for the 2NN–2NN arrangement, various clusters within the 1NN–2NN arrangement display a wide range of shapes, stabilities, and discrete location preferences in the neighborhood of misfit dislocations. As an example, for all dopants considered within the 1NN–2NN arrangement, cluster 6 is the most stable, whereas cluster 1 is found to be the least stable.

Figure 4. *In order to highlight the dispersion in energetics, few stable* M–$V_O^{\cdot\cdot}$–M *clusters with 2NN–2NN arrangement in the vicinity of Layer-1 (interface layer) are illustrated. Only one atomic plane on each side of the interface is shown for clarity. However, in cases where dopant(s) in a particular cluster are either in Layer-2 or Layer-3, they are included in the frame. In certain cases, the same dopant is a constituent of two different clusters. The view is normal to the interface plane. In a given* M–$V_O^{\cdot\cdot}$–M *cluster of the same color, sphere with black border and number signify oxygen vacancy, whereas the corresponding trivalent dopants are denoted by spheres of same color and connected with dashed lines. For each*

dopant species, the energy (eV) for a particular cluster of the respective number is given in ***Table 1****. Color scheme for Ce, Mg, and O ions is shown below the figure.*

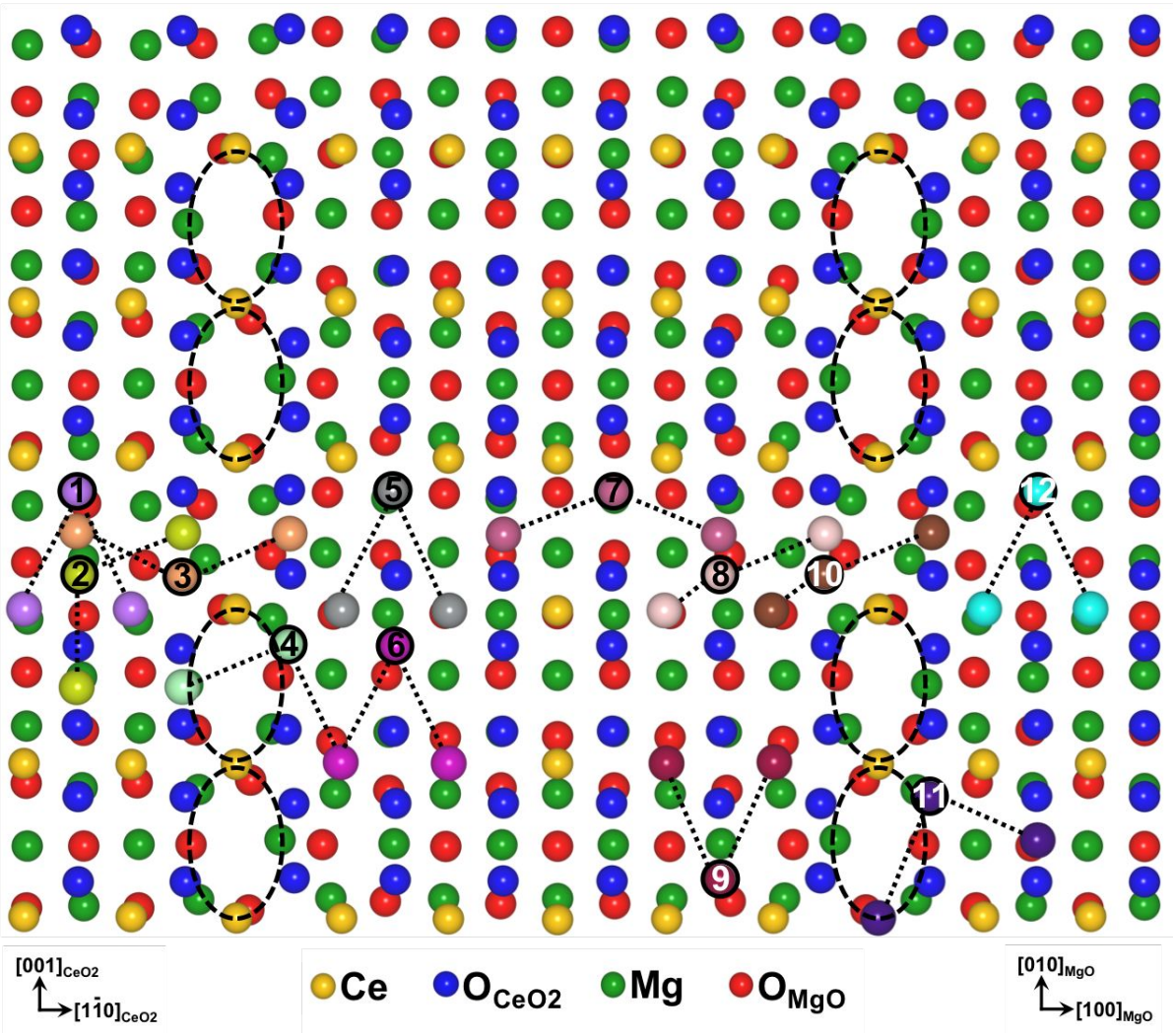

Akin to the trends uncovered for 2NN–2NN (**Figure 4**) and 1NN–2NN (**Figure S1**) arrangements within YDC, GDC, SDC, and LDC, rest of the *x*NN-*y*NN arrangements exhibit clusters with a wide range of stabilities (**Figure 3**); their structures are not shown for brevity. In general, all the *x*NN–*y*NN arrangements in Layer-1 are energetically more stable than their bulk counterpart, even though the energy difference is marginal in some cases, indicating that the interface contains neighborhoods that are energetically favorable for a wide variety of M–$V_{\ddot{O}}$–M clusters. This general behavior reveals that while clusters would prefer the interface, there are few sites at which they can be easily accommodated. That is, although roughly all sites are lower in energy at the interface than in the bulk, there is

substantial gain in energy for placing the cluster at very specific sites. Essentially, the large spread in energies among the different arrangements implies that extended structures are rather favorable at the interface compared to the bulk. Although nearly all clusters are more favorable at the interface than in the bulk, the preference for a particular arrangement is greater at the interface emphasizing the contrasting stability of $M–V_{\ddot{O}}–M$ clusters in the vicinity of misfit dislocations. Overall, at misfit dislocations, the inhomogeneous atomic structure, asymmetry, strain, and availability of diverse nearest neighbor bonding environment is responsible for dispersion in energies of various clusters within a given arrangement.

Table 1. *Energy (eV) for the respective $M–V_{\ddot{O}}–M$ cluster number with 2NN–2NN arrangement in Layer-1, as shown in **Figure 4**. For various trivalent dopants, corresponding structure number for several representative cases are shown in **Figure 4**. Energies are scaled so that 0.0 eV indicates the most favorable cluster arrangement.*

***M–$V_{\ddot{O}}$–M* cluster number**	**Y (eV)**	**Gd (eV)**	**Sm (eV)**	**La (eV)**
1	0.0	0.0	0.0	0.01
2	4.09	4.20	4.31	4.71
3	3.89	3.94	4.0	4.38
4	1.09	1.22	1.33	1.80
5	3.38	3.53	3.64	4.06
6	0.51	0.57	0.60	0.82
7	3.66	3.66	3.70	4.0
8	1.85	1.93	2.0	2.46
9	1.67	1.81	1.85	2.12
10	2.03	2.14	2.25	2.72
11	3.62	3.63	3.59	3.85
12	0.0	0.0	0.0	0.0

3.3 Stability of dopant-defect clusters in Layer-2 of the CeO_2 thin film

In oxide heterostructures, the influence of the interface often extends beyond the interface layer. We have studied the thermodynamic stabilities of M–$V_{\ddot{O}}$–M clusters farther from the interface in order to assess the impact of misfit dislocations. As discussed above, the M–$V_{\ddot{O}}$–M clusters are expected to have extended structures in Layer-1. Herein, we studied the stability of clusters in Layer-2, which is one atomic layer farther from the interface layer (Layer-1). As defined in Section 2, placement of clusters in Layer-2 denote that oxygen vacancies are precisely in Layer-2, but the accompanying dopants could be present in either Layer-1, Layer-2 or Layer-3. Energy ranges for various M–$V_{\ddot{O}}$–M clusters having different *x*NN–*y*NN arrangements in the bulk and in Layer-2 of the thin film are given in **Figure 5**. Bulk values provided for comparison are same as given in **Figure 3**. In Layer-1, 2NN–2NN was the most favorable arrangement for all the dopants. On the contrary, in Layer-2 (**Figure 5**), 2NN–2NN, 1NN–2NN, 2NN–3NN and 1NN–2NN are found to be most favorable arrangement for YDC, GDC, SDC, and LDC, respectively. In Layer-2, clusters with 3NN–3NN arrangement are found to be the least favorable across all dopants.

Similar to Layer-1, spread in energies (**Figure 5)** demonstrate that for a given *x*NN–*y*NN arrangement in YDC, GDC, SDC, and LDC, the energies of various clusters with the same arrangement vary greatly in Layer-2. Nevertheless, this non-homogeneity in energies is somewhat different than that observed in Layer-1, as it reveals that within Layer-2, there are neighborhoods that are both energetically favorable and unfavorable (**Figure 5**) for cluster accommodation as compared to the bulk. Fundamentally, this outcome demonstrates that majority of the locations in Layer-1 are favorable, whereas in Layer-2, some locations are conducive for clusters while others are not. So as to interpret the observed non-homogeneity in energies, analysis similar to the one described earlier for Layer-1 was conducted. For brevity, these structures are not shown here, but the trends are reported. Analogous to Layer-1, lowest energy M–$V_{\ddot{O}}$–M clusters for all the dopants exhibit preference for distinct locations in Layer-2. Similar to the tendencies uncovered for Layer-1, various *x*NN-*y*NN arrangements exhibit clusters with a wide range of stabilities and shapes. As compared to the bulk, noticeable spread in energies among different arrangements reveal that extended structures are thermodynamically favorable in Layer-2, which was also true for Layer-1.

Figure 5. *Energy ranges for various M–$V_O^{\cdot\cdot}$–M cluster arrangements in the bulk and at Layer-2 of the CeO_2 thin film. Ce^{4+} ions are replaced by trivalent dopants Y^{3+}, Gd^{3+}, Sm^{3+}, and La^{3+}. Vertical bars represent the spread in energy (eV) for the various xNN–yNN arrangements indicated by different colors for each trivalent dopant. Energies are scaled so that 0.0 eV indicates the most favorable xNN–yNN arrangement of the M–$V_O^{\cdot\cdot}$–M cluster.*

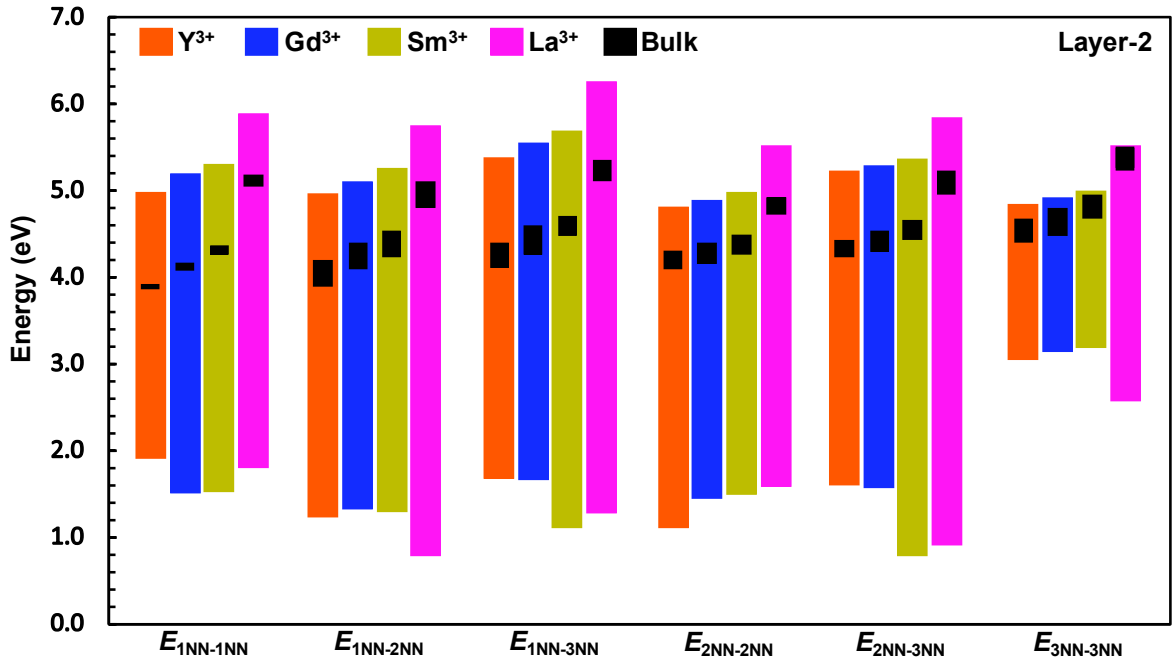

4. Discussion

Key results achieved in this study are: (i) Prediction of atomic-scale structure of misfit dislocations in CeO_2/MgO heterostructure and elucidation of the experimentally observed mixed epitaxial relationship (ii) Evaluation of the thermodynamic stabilities of a wide range of dopant-defect clusters at the CeO_2/MgO interface. Herein, we further discuss the predicted interface structure to facilitate comparison with experimental studies and elucidate the fundamental reasons for the observed stability trends of various dopant-defect clusters, precisely at the interface (Layer-1) and one atomic layer farther from the interface (Layer-2). Finally, we consider the implications of these results on ionic conductivity in ceria-based thin film electrolytes.

Several experimental studies have reported the cube-on-cube epitaxial relationship between ceria-based thin films (ceria, GDC, SDC) and MgO substrates,[77,78,79,80,81,82] whereas few experiments have observed mixed epitaxy with an in-plane orientation

relationship of $[100]_{CeO2}||[010]_{MgO}$ and $[110]_{CeO2}||[100]_{MgO}$.[78,82] Besides, in the cube-on-cube epitaxy, evidence of local isolated domains rotated by 45º around the substrate surface normal has been reported.[79] We elucidate from a fundamental perspective, the experimentally observed mixed epitaxial relationship, which is also used in the present study. In the CeO_2 $[001]$ direction, alternating planes of Ce and O atoms are accountable for the dipole along the $[001]$ surface.[100] The CeO_2/MgO heterostructures assembled using cube-on-cube epitaxial relationship will have the possibility of either Ce or O terminated planes, either of which will lead to the presence of surface dipole. In order to eliminate the surface dipole, we have rotated the CeO_2 thin film by 45° (**Figure 1**), which lead to the mixed epitaxial relationship observed in experiments.[78,82] Our results reveal that the 45º rotation of CeO_2 thin film is one of the potential fundamental mechanisms to eliminate the surface dipole and render greater stability to the heterostructure.

In experiments that report the cube-on-cube epitaxial relationship, surface dipole could be one potential reasons for the lower quality films,[79] as well as the presence of rectangular grains in surface and columnar grains in cross section.[80] Besides, the formation of defects such as steps at the CeO_2/MgO interface could potentially eliminate the surface dipole, but lead to rough interfaces.[77,78] Our previous work on polar pyrochlores surfaces demonstrated that formation of steps and trenches are potential mechanisms to eliminate surface dipole.[101] In addition, for the CeO_2/MgO system, Copetti *et al*.[78] reported that the thin film nucleation on steps lead to CeO_2[100] orientation, whereas nucleation on terraces lead to CeO_2[110] orientation. Similarly, Chen *et al*.[77] reported the occurrence of steps at the CeO_2/MgO interface for cube-on-cube epitaxy. It is imperative to note that there are other probable mechanisms that could eliminate the surface dipole in oxides. For instance, redistribution of ionic charges[102] and charge transfer effects could compensate for macroscopic dipole. In addition, surface dipole in oxides could be negated via structural reconstruction of the terminating layers,[103] the formation of surface oxygen vacancies,[104] and surface rumpling and the electron density redistribution at the surface.[105]

An added benefit of having the mixed termination is that the ~28.4% strain along the CeO_2[100] direction decreases to ~9.1% along the CeO_2[110] direction. That said, the decrease in strain is not the central reason for the mixed epitaxial relationship, because the elimination of the surface dipole is critical from a fundamental perspective. If strain reduction was the only driving factor, CeO_2 thin film would have preferred a rotation parallel to the

MgO substrate so that the strain along the CeO_2[110] and CeO_2[011] directions is reduced to ~9.1%, in which case the surface dipole would nevertheless be present due to either Ce or O termination. From a basic perspective, our results elucidate that the mixed epitaxial relationship (**Figures 1** and **2**) observed in experiments is responsible for eliminating the surface dipole in CeO_2/MgO heterostructure. Furthermore, we have demonstrated that the decrease in strain along the CeO_2[110] direction lead to a different misfit dislocation structure as compared to the CeO_2[100] direction. A vital feature is that we have established dissimilar misfit dislocation structure along the CeO_2[110] and CeO_2[100] directions, which alleviate the large strain between the mismatched materials as observed in some experiments,[77,79,81] but not in others.[78,80,82] In experimental studies that do not report the formation of misfit dislocations, although the mechanism for strain mitigation is not clear, it is conceivable that the defects observed at the interface play an important role.[82] Atomic-scale details of the CeO_2/MgO interface offered in this work for the mixed epitaxial relationship observed in experiments has not been reported previously. Furthermore, the dissimilar dislocation structure along the two directions of the CeO_2 thin film have not been hitherto established, and offers potential avenues to comprehend the fundamental role of extended defects in influencing the functionality of nanostructured electrolytes assembled using mismatched oxides.

Results pertaining to the stabilities of various dopant-defect clusters are offered in the Results section. In the bulk, energies of a given type of M–$V_{\ddot{O}}$–M cluster arrangement do not vary significantly, less than 0.35 eV in all cases and typically much less. In contrast, the CeO_2/MgO interface induces considerable dispersion in energies demonstrating that there is a wide range of energies for different clusters of the same arrangement at the interface. An important trend uncovered is that 2NN–2NN is the most favorable arrangement in Layer-1 (**Figure 3)** for all the dopants, whereas in Layer-2 (**Figure 5**), 2NN–2NN, 1NN–2NN, 2NN–3NN, and 1NN–2NN are found to be most favorable arrangement for YDC, GDC, SDC, and LDC, respectively. Remarkably, these findings highlight the disparity in favorable cluster arrangements that are separated by one atomic layer. It implies that while the most favorable cluster arrangement at the interface is same for all the trivalent dopants considered, this preference is likely to change depending on the distance from the interface. Most stable clusters within Layer-2 are less favorable than the most stable clusters in Layer-1 by roughly 0.66–1.31 eV, indicating that the influence of misfit dislocations at the interface

diminishes farther from the interface. Another common feature apparent in **Figures 3** and **5** is that favorable M–$V_O^{\cdot\cdot}$–M cluster arrangements in Layer-1 and Layer-2 do not necessarily resemble those located in the bulk, revealing that evaluating the structure of clusters in the bulk is not sufficient to characterize their structure at heterointerfaces. These key findings reveal that the most favorable M–$V_O^{\cdot\cdot}$–M cluster at the interface is characteristically different than in the bulk owing to the influence of misfit dislocations and strain at the interface. In general, due to strong binding between defects and dopants in these complexes, they are expected to be bound at the interface as well. That is, position of the dopants and defects will not be independent at the interface, just as they are not in the bulk. Hence, the wide variety of M–$V_O^{\cdot\cdot}$–M clusters examined in this work are essential to elucidate the intricate role of misfit dislocations in influencing oxygen vacancy formation and diffusion in doped ceria-based thin films.

For all the dopants, a common behavior observed is the non-homogeneity in energies for different clusters within the same arrangement, which can best be understood by taking a closer look at the interface atomic stacking and the nearest neighbor bonding across the interface. For dopant-defect clusters with the 2NN–2NN arrangement (**Figure 4** and **Table 1**) in Layer-1, we find that all trivalent dopants exhibit tendencies to be in Layer-1, as compared to Layer-2. This result is a consequence of greater available space at the interface plane, which can easily accommodate larger trivalent dopants. For instance, clusters 4 and 11 have one dopant in Layer-2 and the other in Layer-1, whereas clusters 2, 3, 7, 8, and 10 have both dopant atoms in Layer-2, all of which have lower stability. On the contrary, greater stability is exhibited by clusters 1, 6, and 12, which have both dopants in Layer-1 indicating that clusters with 2NN–2NN arrangement having larger dopants in Layer-1 are more stable. On the contrary, clusters 5 and 9 also have both the dopants in Layer-1, but exhibit lower stability. This discrepancy can be primarily attributed to the site of oxygen vacancy. In clusters 1 and 12, oxygen atom in CeO_2 is located right on top of oxygen atom in MgO. Due to this repulsive electrostatic interaction, formation of oxygen vacancy in clusters 1 and 12 is favorable along with the fact that both the dopants are in Layer-1, which render them the greatest stability. In cluster 5, although both dopants are in Layer-1, the oxygen atom is right on top of an Mg ion. Removal of an oxygen atom from this region of attractive electrostatic interaction lead to lower stability.

Analogous to the 2NN–2NN arrangement, for dopant-defect clusters with 1NN–2NN arrangement (**Figure S1** and **Table S1**) in Layer-1, we find that all trivalent dopants exhibit propensities to be in Layer-1, as compared to Layer-2. For instance, cluster 1, which has both the dopants in Layer-2 displays the lowest stability, whereas clusters 4, 5, 6, 7, and 10 having both dopants in Layer-1 demonstrate greater stability. Similar tendencies are observed in other *x*NN–*y*NN arrangements. In general, larger trivalent dopants prefer Layer-1 due to additional space and diverse bonding environment available at the interface, but their strong binding with oxygen vacancies reveal that the location of oxygen vacancy formation is critical for the stability of M–$V_{\ddot{O}}$–M clusters.

Among the various trivalent dopants considered in this work, cluster stability trend in terms of maximum energy difference between the interface (Layer-1) and the bulk (**Figure 3**) can be given as: LDC > SDC > GDC > YDC. This trend implies that the clusters in LDC exhibit stronger propensity to segregate at the interface as compared to the other dopants. A fundamental explanation for the observed trend is found in the increasing trend in ionic radii: La^{3+}(0.103) > Sm^{3+}(0.096) > Gd^{3+}(0.094) > Y^{3+}(0.09) > Ce^{4+}(0.087); where the values in parenthesis are ionic radii in nm for six-fold coordination as given by Shannon.[106] The size disparity between the trivalent dopants and the host cations (Ce^{4+}) is evident, wherein all the dopants are larger than Ce^{4+}. However, the size mismatch between La^{3+} and Ce^{4+} is the maximum, revealing that the reduction in elastic strain energy at the interface would be more prominent if clusters comprising La^{3+} dopants are located at the interface. Since the interface has more open space as compared to the bulk, it can accommodate larger dopants, which is consistent with our results. In general, for M–$V_{\ddot{O}}$–M clusters with diverse *x*NN–*y*NN arrangements within YDC, GDC, SDC, and LDC, the interface (Layer-1) exhibit all locations that are energetically favorable as compared to the bulk. These findings critically emphasize that all locations at the interface are conducive for dopant-defect cluster segregation. Nonetheless, this is not true for Layer-2, where some locations are even less favorable than the bulk. Overall, this trend elucidates that complexes containing trivalent dopants of different ionic size and chemical nature will exhibit variation in stability in the proximity of misfit dislocation at CeO_2/MgO interface.

Considering all the dopants, the most favorable arrangement of M–$V_{\ddot{O}}$–M cluster at the interface (Layer-1) has both the dopants at 2NN to the oxygen vacancy. For Y, Gd, and Sm dopants, these findings are in contrast to the behavior in bulk in the present

calculations, and other theoretical calculations, which report that the most favorable location for oxygen vacancy formation in YDC, GDC, and SDC is 1NN [46,48,57,58,62,65] to one of the dopant ions. However, for La dopants, 2NN is found to be the most favorable location in the bulk.[46,58] Calorimetric measurements also reported a similar preference of oxygen vacancies to remain at 1NN to trivalent dopants such as Gd, Y, and La.[107] Besides, at grain boundaries in nanocrystalline doped ceria, variation from bulk for most favorable oxygen vacancy location was reported.[75] Crucially, our calculations indicate that the favorable cluster arrangements at the CeO_2/MgO interface are different that those in the bulk as well as at grain boundaries. Also, there is a fundamental difference for the local environment in grain boundaries as compared to heterointerfaces. At oxide heterointerfaces, the dopants and defects in a given cluster interact with atoms from a completely different oxide, which is not the case for grain boundaries. As a result, knowledge of the fundamental clusters in the bulk and at grain boundaries in doped ceria might not be sufficient to characterize their influence at misfit dislocations in ceria-based thin films. Furthermore, present findings indicate that the location of the second dopant within a M–$V_{\ddot{O}}$–M cluster, which will be reliant on the cluster location as well as on the dopant type, is imperative to predict its stability, particularly at misfit dislocations. Fundamentally, the large dispersion in energies (**Figures 3** and **5**) for a particular *x*NN–*y*NN cluster arrangement in Layer-1 (interface) and Layer-2 is not expected in the bulk. In other words, as compared to the bulk, the stability of the cluster in the neighborhood of misfit dislocations is much more sensitive to the position of the second dopant. Consequently, studying the fundamental M–$V_{\ddot{O}}$ dimers and M–$V_{\ddot{O}}$–M (trimers) clusters in the bulk, which has been addressed, [46,47,48,56,58,62,65] does not elucidate their behavior at misfit dislocations.

It is critical to note that in addition to the most favorable 2NN–2NN arrangement of M–$V_{\ddot{O}}$–M clusters dwelling in the vicinity of misfit dislocations, numerous other *x*NN–*y*NN cluster arrangements would exist near the interface contingent on their energetics and the fraction of available sites. This is due to the fact that all clusters within the different arrangements are stable at the interface (Layer-1) than in the bulk (**Figure 3**), but only few locations are very stable. Once these locations are occupied, other sites would start filling up, which might necessitate different types of arrangement. Besides, clusters may also encounter stable locations in Layer-2, wherein certain sites are very stable while others are not (**Figure 5**). In general, a rather complicated distribution of diverse clusters is probable

near the interface. An important feature inferred from comparing the behavior of dopant-defect complexes at the interface versus bulk is the greater preference for a specific arrangement at the interface. Within the bulk, energy differences between the lowest energy cluster for different arrangements are rather modest. At the interface, these differences are significantly higher. Disparities in stabilities between the dissimilar arrangements are linked to the binding of the dopant-defect cluster, indicating that the binding of oxygen vacancies to dopants in the vicinity of misfit dislocations is stronger than in the bulk, which is expected to impact the mobility of oxygen vacancies at the interface. As displayed in **Figures 4** and **S1**, the stability of the cluster depends heavily not only on the location of the oxygen vacancy, but also on the local arrangement of dopants, revealing that the stability of oxygen vacancy is much more sensitive to the dopant arrangement near misfit dislocations than in the bulk. As a result, the binding of oxygen vacancies to dopants is rather complicated at the interface, and is expected to be influenced by the distribution of dopants.

It is imperative to note that throughout this study, we have only considered one cluster at any given instant, not accounting for the influence of other clusters. At higher dopant fractions, the possibility of several disparate clusters agglomerating at the interface cannot be denied. For instance, for a given most favorable dopant-defect cluster with 2NN-2NN arrangement, the dopants therein could have additional oxygen vacancies at 1NN or 3NN, or the 2NN-2NN arrangement could have additional dopants at 1NN or 3NN that are associated with other clusters. Additionally, to identify a particular cluster, we have strictly located oxygen vacancies in the CeO_2 side of the interface. Nevertheless, it is quite possible that oxygen vacancies are present on the MgO side of the interface as well, which could further influence the stabilities of the dopant-defect clusters at the interface (Layer-1). The stabilities of coexisting clusters would be strongly influenced by cluster-cluster interactions. Consequently, there could be numerous overlapping $M\text{–}V_O^{\cdot\cdot}\text{–}M$ clusters present in the vicinity of the interface, which would impact the cluster stabilities, and further complicate the energetic landscape of oxygen vacancies. Nonetheless, by rigorously investigating isolated $M\text{–}V_O^{\cdot\cdot}\text{–}M$ clusters in the CeO_2 thin film, present work offers fundamental insights into their stabilities as a function of dopant type and oxygen vacancy location, and shed light on the influence of misfit dislocations in ceria-based thin films and heterostructures.

As discussed in the Introduction, there are several experiments that report enhanced ionic conductivity at misfit dislocations in oxides, [7,8,9,16,17,18,19,20,21,22] whereas few reports

suggest that there is no such influence of misfit dislocations. [23,24,42,43,44,45] As reported in the present calculations, compared to the bulk, enhanced thermodynamic stabilities of diverse clusters at misfit dislocations is expected to impact the overall oxide ion conductivity in doped ceria-based thin films. As discussed above, the M–$V_O^{\cdot\cdot}$–M clusters are strongly bound at the interface, more so than they are in the bulk. [46,47,48,57] Greater stability of dopant-defect clusters at the interface would lead to high concentration of dopants and defects in the vicinity of misfit dislocations. As a result, ionic conductivity is expected to increase due to high carrier (oxygen vacancy) concentration. Nonetheless, similar to the trend in ionic conductivity observed in the bulk of doped ceria, [46,47,48,56,57,62,64,65] owing to the high fraction of trivalent dopants due to segregation and the strong dopant-defect binding at the CeO_2/MgO interface, blocking of mobile carriers is very likely, leading to a decrease in ionic conductivity. Thus, competing effects would exist, especially in the neighborhood of misfit dislocations. These potentially opposing effects of dopant-defect cluster stability on ionic conductivity at misfit dislocations in ceria-based thin films may be responsible for the conflicting experimental findings for misfit dislocations in oxide thin films. It is imperative to note that the present work is exclusively focused on defect thermodynamics, without any information of defect kinetics. To fully appreciate the fundamental role of misfit dislocations in thin film oxide electrolytes, a more comprehensive modeling effort that tackles defect diffusion in the vicinity of dopants is necessitated, which will be addressed in future work.

5. Conclusions

We have predicted the atomic-scale structure of misfit dislocations in CeO_2/MgO heterostructures. From a fundamental perspective, the mixed epitaxial relationship observed in experiments for CeO_2/MgO heterostructures is elucidated on the basis of our results, which reveal that the 45º rotation of CeO_2 thin film is one of potential fundamental mechanisms to eliminate the surface dipole and render greater stability to the heterostructure. We have established dissimilar misfit dislocation structure along the CeO_2[110] and CeO_2[100] directions. Atomic-scale details of the CeO_2/MgO interface and the dissimilar dislocation structure along the two directions of the CeO_2 thin film have not been hitherto established. We have further examined the thermodynamic stabilities of various geometrically and energetically dissimilar dopant-defect clusters at the interface. These clusters exhibit widespread dispersion in energies within the same arrangement, and

are in general found to exhibit greater stability at the interface as compared to the bulk. Our findings reveal that misfit dislocations at the interface strongly influence cluster stability, and the thermodynamic stability of the oxygen vacancy is sensitive to the dopant arrangement at the heterointerface. Present findings also highlight the disparity in favorable dopant-defect cluster arrangements that are separated by one atomic layer from the interface layer, which can be attributed to the strong influence of misfit dislocations at the interface layer. It is further revealed that the fundamental structure of the preferred dopant-defect clusters at the interface is characteristically different than in the bulk owing to the influence of misfit dislocations and strain at the interface. In CeO_2/MgO heterostructures, greater stability of clusters at misfit dislocations is expected to lead to opposing effects, wherein additional carriers at the interface will enhance ionic conductivity, but their mobility is expected to be sluggish due to the inhomogeneous atomic structure of misfit dislocations and stronger dopant-defect binding, which in turn will decrease conductivity. Present results underpin the importance of understanding the atomic-scale structure of misfit dislocations and offers potential avenues to comprehend the fundamental role of extended defects in influencing the functionality of oxide electrolytes synthesized using mismatched oxides. Finally, our work further assists in disentangling the multifaceted role of dopants and defects in influencing ionic transport in oxide thin films and heterostructures.

Acknowledgments

P.P.D. wishes to acknowledge the Startup Funds provided by the College of Science, Rochester Institute of Technology. This work used the Extreme Science and Engineering Discovery Environment (XSEDE), which is supported by National Science Foundation grant number ACI-1548562.

References

[1] P. Zubko, S. Gariglio, M. Gabay, P. Ghosez and J.-M. Triscone, *Annu. Rev. Cond. Matt. Phys.*, 2011, **2**, 141.

[2] J. A.Sulpizio, S. Ilani, P. Irvin and J. Levy, *Annu. Rev. Mater. Res.*, 2014, **44**, 117.

[3] N. Pryds and V. Esposito, *J. Electroceram.*, 2017, **38**, 1.

[4] P. Yu, Y.-H. Chu and R. Ramesh, *Mater. Today*, 2012, **15**, 320.

[5] Z. Huang, Ariando, X. R. Wang, A. Rusydi, J. Chen, H. Yang and T. Venkatesan, *Adv. Mater.*, 2018, **30**, 1802439.

[6] H. Y. Hwang, Y. Iwasa, M. Kawasaki, B. Keimer, N. Nagaosa and Y. Tokura, *Nat. Mater.*, 2012, **11**, 103.

[7] E. Fabbri, D. Pergolesi and E. Traversa, *Sci. Tech. Adv. Mater.*, 2010, **11**, 054503.

[8] J. Garcia-Barriocanal, A. Rivera-Calzada, M. Varela, Z. Sefrioui, E. Iborra, C. Leon, S. J. Pennycook and J. Santamaria, *Science*, 2008, **321**, 676.

[9] M. Sillassen, P. Eklund, N. Pryds, E. Johnson, U. Helmersson and J. Bøttiger, *Adv. Func. Mater.*, 2010, **20**, 2071.

[10] F. Zhang, H. Cao, D. Yue, J. Zhang and M. Qu, *Inorgan. Chem.*, 2012, **51**, 9544.

[11] I. J. Beyerlein, M. J. Demkowicz, A. Misra and B. P. Uberuaga, *Prog. Mater. Sci.*, 2015, **74**, 125.

[12] H. Jeen, W. S. Choi, M. D. Biegalski, C. M. Folkman, I.-C. Tung, D. D. Fong, J. W. Freeland, D. Shin, H. Ohta, M. F. Chisholm and H. N. Lee, *Nat. Mater.*, 2013, **12**, 1057.

[13] E. Assmann, P. Blaha, R. Laskowski, K. Held, S. Okamoto and G. Sangiovanni, *Phys. Rev. Lett.*, 2013, **110**, 078701.

[14] M. Salluzzo, S. Gariglio, D. Stornaiuolo, V. Sessi, S. Rusponi, C. Piamonteze, G. M. De Luca, M. Minola, D. Marre, A. Gadaleta, H. Brune, F. Nolting, N. B. Brookes and G. Ghiringhelli, *Phys. Rev. Lett.*, 2013, **111**, 087204.

[15] S. Pennycook, H. Zhou, M. Chisholm, A. Borisevich, M. Varela, J. Gazquez, T. Pennycook and J. Narayan, *Acta Mater.*, 2013, **61,** 2725.

[16] N. Schichtel, C. Korte, D. Hesse and J. Janek, *Phys. Chem. Chem. Phys*., 2009, **11**, 3043.

[17] A. Peters, C. Korte, D. Hesse, N. Zakharov and J. Janek, *Solid State Ion.*, 2007, **178**, 67.

[18] V. Sadykov, V. Usoltsev, N. Yeremeev, N. Mezentseva, V. Pelipenko, T. Krieger, V. Belyaev, E. Sadovskaya, V. Muzykantov, Y. Fedorova, A. Lukashevich, A. Ishchenko, A. Salanov, Y. Okhlupin, N. Uvarov, O. Smorygo, A. Arzhannikov, M. Korobeynikov and M. Thumm, *J. Euro. Ceram. Soc*., 2013, **33,** 2241.

[19] S. Lee, W. Zhang, F. Khatkhatay, H. Wang, Q. Jia and J. L. MacManus-Driscoll, *Nano Lett*., 2015, **15,** 7362.

[20] I. Kosacki, C. M. Rouleau, P. F. Becher, J. Bentley and D. H. Lowndes, *Solid State Ion.*, 2005, **176**, 1319.

[21] D. Pergolesi, M. Fronzi, E. Fabbri, A. Tebano and E. Traversa, *Mater. Renew. Sust. Energy*, 2012, **2**, 6.

[22] Y. Saito, J. Cheng, K. Crabb, H. Huang, R. Pornprasertsuk, P. C. Su and F. Prinz, *ECS Trans*., 2008, **11**, 3.

[23] X. Guo, *Science*, 2009, **324**, 465.

[24] G. F. Harrington, A. Cavallaro, D. W. McComb, S. J. Skinner and J. A. Kilner, *Phys. Chem. Chem. Phys*., 2017, **19**, 14319.

[25] P. P. Dholabhai, E. Martinez, N. T. Brown and B. P. Uberuaga, *Phys. Chem. Chem. Phys.,* 2017, **19**, 23122.

[26] P. P. Dholabhai, G. Pilania, J. A. Aguiar, A. Misra and B. P. Uberuaga, *Nat. Commun*., 2014, **5**, 5043.

[27] B. P. Uberuaga, E. Martinez, Z. Bi, M. Zhuo, Q. Jia, M. Nastasi, A. Misra and A. Caro, *Mater. Res. Lett*., 2013, **1**, 193.

[28] P. P. Dholabhai, J. A. Aguiar, A. Misra and B. P. Uberuaga, *J. Chem. Phys*., 2014, **140**, 194701.

[29] J. A. Aguiar, P. P. Dholabhai, Z. Bi, Q. Jia, E. Fu, Y. Wang, T. Aoki, J. Zhu, A. Misra and B. P. Uberuaga, *Adv. Mater. Inter*. 2014, **1**, 1300142.

[30] V. Nagarajan, C. L. Jia, H. Kohlstedt, R. Waser, I. B. Misirlioglu, S. P. Alpay and R. Ramesh, *Appl. Phys. Lett*., 2005, **86**, 192910.

[31] Y. B. Xu, Y. L. Tang, Y. L. Zhu, Y. Liu, S. Li, S. R. Zhang and X. L. Ma, *Sci. Rep*., 2016, **6**, 35172.

[32] W.-J. Lee, H. J. Kim, J. Kang, D. H. Jang, T. H. Kim, J. H. Lee and K. H. Kim, *Annu. Rev. Mater. Res*., 2017, **47**, 391.

[33] N. Bagués, J. Santiso, B. D. Esser, R. E. A. Williams, D. W. McComb, Z. Konstantinovic, L. Balcells and F. Sandiumenge, *Adv. Func. Mater*., 2018, **28***,* 1704437.

[34] B. Yildiz, *MRS Bulletin*, 2014, **39**, 147.

[35] F. Sandiumenge, *J. Mater. Res.*, 2017, **32**, 3958.

[36] A. Jaiswal, A. Pesaran, S. Omar, and E. D. Wachsman, *ECS Transac.*, 2017, **78**, 361.

[37] E. D. Wachsman and K. T. Lee, *Science*, 2011, **334**, 935.

[38] J. A. Kilner and M. Burriel, *Annu. Rev. Mater. Res*. 2014, **44**, 11.1−11.29.
[39] D. J. L. Brett, A. Atkinson, N. P. Brandon, and S. J. Skinner, *Chem. Soc. Rev.*, 2008, **37**, 1568–1578.

[40] A. Lashtabeg and S. J. Skinner, *J. Mater. Chem.*, 2006, **16**, 3161–3170.

[41] S. J. Skinner, S. Cook and J. A. Kilner, 2013, 181–201, Materials for Next Generation SOFCs. In: J. Irvine, P. Connor (eds) Solid Oxide Fuels Cells: Facts and Figures. Green Energy and Technology. Springer, London.

[42] B. Li, J. Zhang, T. Kaspar, V. Shutthanandan, R. C. Ewing and J. Lian, *Phys. Chem. Chem. Phys*., 2013, **15**, 1296.

[43] X. Guo, E. Vasco, S. Mi, K. Szot, E. Wachsman and R. Waser, *Acta Mater.*, 2005, **53**, 5161.

[44] L. Sun, D. Marrocchelli and B. Yildiz, *Nat. Commun*., 2015, **6**, 6294.

[45] V. Metlenko, A. H. H. Ramadan, F. Gunkel, H. Du, H. Schraknepper, S. Hoffmann-Eifert, R. Dittmann, R. Waser and R. A. De Souza, *Nanoscale*, 2014, **6**, 12864.

[46] D. A. Andersson, S. I. Simak, N. V. Skorodumova, I. A. Abrikosov and B. Johansson, *Proc. Nat. Acad. Sci.*, 2006, **103**, 3518.

[47] P. P. Dholabhai, J. B. Adams, P. Crozier and R. Sharma, *J. Chem. Phys*., 2010, **132**, 094104.

[48] P. P. Dholabhai, J. B. Adams, P. Crozier and R. Sharma, *Phys. Chem. Chem. Phys*., 2010, **12**, 7904.

[49] H. L. Tuller and A. S. Nowick, *J. Electrochem. Soc.*, 1975, **122**, 255.

[50] B. C. H. Steele, *Solid State Ion.*, 2000, **129**, 95.

[51] H. L. Tuller, *Solid State Ion.*, 2000, **131**, 143.

[52] M. Mogensen, N. M. Sammes and G. A. Tompsett, *Solid State Ion.*, 2000, **129**, 63.

[53] S. Omar, E. D. Wachsman, and J. C. Nino, *Appl. Phys. Lett.*, 2007, **91**, 1444106.

[54] B. C. H. Steele and A. Heinzel, *Nature,* 2001, **414**, 345.

[55] B. C. H. Steele, *Solid State Ion.,* 2000, **134**, 3.

[56] P. P. Dholabhai, S. Anwar, J. B. Adams, P. Crozier and R. Sharma, *J. Solid State Chem.*, 2011, **184**, 811.

[57] M. Nakayama and M. Martin, *Phys. Chem. Chem. Phys*., 2009, **11**, 3241.

[58] S. Grieshammer, B. O. H. Grope, J. Koettgen, and M. Martin, *Phys. Chem. Chem. Phys*., 2014, **16**, 9974.

[59] S. Grieshammer, M. Nakayama and M. Martin, *Phys. Chem. Chem. Phys*., 2016, **18**, 3804.

[60] S. Grieshammer and M. Martin, *J. Mater. Chem. A*, 2017, **5**, 9241.

[61] J. Koettgen, P. C. Schmidt, T. Bucko and M. Martin, *Phys. Rev. B*, 2018, **97**, 024305.

[62] J. Koettgen, S. Grieshammer, P. Hein, B. O. H. Grope, M. Nakayama and M. Martin, *Phys. Chem. Chem. Phys*., 2018, **20**, 14291.

[63] J. Koettgen and M. Martin, *J. Phys. Chem. C*, 2019, **123**, 6333.

[64] P. P. Dholabhai, S. Anwar, J. B. Adams, P. A. Crozier and R. Sharma, *Modelling Simul. Mater. Sci. Eng*. 2012, **20**, 015004.

[65] P. P. Dholabhai and J. B. Adams, *J. Mater. Sci*. 2012, **47**, 7530.

[66] K. Hirai, R. Aso, Y. Ozaki, D. Kan, M. Haruta, N. Ichikawa, H. Kurata and Y. Shimakawa, *ACS Appl. Mater. Inter*., 2017, **9**, 30143.

[67] P. P. Dholabhai, E. Martinez and B. P. Uberuaga, *Adv. Theory Simul*., 2019, **2**, 1800095.

[68] W. L. Cheah and M. W. Finnis, *J. Mater. Sci*., 2012, **47**, 1631.

[69] A. I. Abutaha, S. R. Sarath Kumar, A. Mehdizadeh Dehkordi, T. M. Tritt and H.N. Alshareef, *J. Mater. Chem. C,* 2014, **2**, 9712.

[70] X. Aparicio-Angles and N. H. de Leeuw, *J. Am. Ceram. Soc.,* 2017, **100**, 3329.

[71] B. W. Veal, S. K. Kim, P. Zapol, H. Iddir, P. M. Baldo and J. A. Eastman, *Nature Comm.*, 2016, **7**, 11892.

[72] G. Herranz, M. Basletic, M. Bibes, C. Carretero, E. Tafra, E. Jacquet, K. Bouzehouane, C. Deranlot, A. Hamzic, J.-M. Broto, A. Barthelemy and A. Fert, *Phys. Rev. Lett*., 2007, **98**, 216803.

[73] U. Dey, S. Chatterjee and A. Taraphder, *Phys. Chem. Chem. Phys.*, 2018, **20**, 17871.

[74] Y. Y. Zhang, R. Mishra, T. J. Pennycook, A. Y. Borisevich, S. J. Pennycook and S. T. Pantelides, *Adv. Mater. Inter*., 2015, **2**, 1500344.

[75] P. P. Dholabhai, J. A. Aguiar, L. Wu, T. G. Holesinger, T. Aoki, R. H. R. Castro and B. P. Uberuaga, *Phys. Chem. Chem. Phys.,* 2015, **17**, 15375.

[76] Z.-P. Li, T. Mori, F. Ye, D. Ou, J. Zou and J. Drennan, *J. Chem. Phys.* 2011, **134**, 224708.

[77] L. Chen, C. L. Chen, X. Chen, W. Donner, S. W. Liu, Y. Lin, D. X. Huang and A. J. Jacobson, *Appl. Phys. Lett.*, 2003, **83**, 4737.

[78] C. A. Copetti, J. Schubert, A. M. Klushin, S. Bauer, W. Zander, Ch. Buchal, J. W. Seo, F. Sanchez and M. Bauer, *J. Appl. Phys.*, 1995, **78**, 5058.

[79] A. Fluri, D. Pergolesi, V. Roddatis, A. Wokaun and T. Lippert, *Nat. Comm.,* 2016, **7**, 10692.

[80] P. Zhao, Z. Huang, Y. Mao, Y. Wang and G. Takashi, *Ceram. Inter.,* 2014, **40**, 15919.

[81] S. Sanna, V. Esposito, J. W. Andreasen, J. Hjelm, W. Zhang, T. Kasama, S. B. Simonsen, M. Christensen, S. Linderoth and N. Pryds, *Nat. Mater.,* 2015, **14**, 500.

[82] R. Perez Casero, R. Gomez San Roman, J. Perriere, A. Laurent, W. Seiler, P. Gergaud and D. Keller, *Appl. Surf. Sci*., 1997,**109**/**110**, 341.

[83] P. P. Dholabhai and B. P. Uberuaga, *Adv. Theory Simul.* Accepted for Publication

[84] C. Cheng, K.Kunc, G. Kresse and J. Hafner, *Phys. Rev. B*, 2002, **66**, 085419.

[85] P. Casek, S. Bouette-Russo, F. Finocchi and C. Noguera, *Phys. Rev. B,* 2004, **69**, 085411.

[86] P. Casek, F. Finocchi and C. Noguera, *Phys. Rev. B*, 2005, **72**, 205308.

[87] T. J. Pennycook, M. J. Beck, K. Varga, M. Varela, St. J. Pennycook and S. T. Pantelides, *Phys. Rev. Lett.*, 2010, **104**, 115901.

[88] S. Plimpton, *J. Comput. Phys*., 1995, **117**, 1.

[89] R. A. Buckingham, *Proc. R. Soc. London, Ser. A*, 1938, **168**, 264.

[90] P. P. Ewald, *Ann. Phys*., 1921, **64**, 253.

[91] G. Busker, A. Chroneos, R. W. Grimes and I. Chen, *J. Am. Ceram. Soc*., 1999, **82**, 1553.

[92] L. Minervini, M. O. Zacate and R. W. Grimes, *Solid State Ion.*, 1999, **116**, 339.

[93] M. O. Zacate, L. Minervini, D. J. Bradfield, R. W. Grimes and K. E. Sickafus, *Solid State Ion.*, 2000, **128**, 243.

[94] J. Towns, T. Cockerill, M. Dahan, I. Foster, K. Gaither, A. Grimshaw, V. Hazlewood, S. Lathrop, D. Lifka, G. D. Peterson, R. Roskies, J. Ray Scott and N. Wilkins-Diehr, "XSEDE: Accelerating Scientific Discovery", Computing in Science & Engineering, vol.16, no. 5, pp. 62-74, Sept.-Oct. 2014, doi:10.1109/MCSE.2014.80

[95] R. Gerhardt-Anderson and A. S. Nowick, *Solid State Ion*. 1981, **5**, 547.

[96] Md. M. Hasan, P. P. Dholabhai, R. H. R. Castro and B. P. Uberuaga, *Surf. Sci.,* 2016, **649**, 138.

[97] Wu, L.; Aguiar, J. A.; P. P. Dholabhai, T. Holesinger, T. Aoki, B. P. Uberuaga and R. H. R. Castro, *J. Phys. Chem. C*, 2015, **119**, 27855.

[98] P. V. Nerikar, D. C. Parfitt, L. A. C. Trujillo, D. A. Andersson, C. Unal, S. B. Sinnott, R. W. Grimes, B. P. Uberuaga and C. R. Stanek, *Phys. Rev. B*, 2011, **84**, 174105.

[99] Y. Li, P. A. Korzhavyi, R. Sandstrom and C. Lilja, *Phys. Rev. Mater.*, 2017, **1**, 070602(R).

[100] P. W. Tasker, *Philos. Mag. A,* 1979, **39**, 119.

[101] P. P. Dholabhai, R. Perriot and B. P. Uberuaga, *J. Phys. Chem. C*, 2016, **120**, 10485.

[102] J. H. Harding, *Surf. Sci*., 1999, **422**, 87.

[103] M. Setvin, M. Reticcioli, F. Poelzleiter, J. Hulva, M. Schmid, L. A. Boatner, C. Franchini and U. Diebold, *Science*, 2018, **359**, 572.

[104] E. Heifets, W. A. Goddard III, E. A. Kotomin, R. I. Eglitis and G. Borstel, *Phys. Rev. B*, 2004, **69**, 035408.

[105] Y. A. Mastrikov, R. Merkle, E. A. Kotomin, M. M. Kuklja and J. Maier, *J. Mater. Chem. A*, 2018, **6**, 11929.

[106] R. D. Shannon, *Acta Crystallogr., Sect. A: Cryst. Phys., Diffr., Theor. Gen. Crystallogr*., 1976, **32**, 751.

[107] A. Navrotsky, P. Simoncic, H. Yokokawa, W. Chen and T. Lee, *Faraday Discuss*., 2007, **134**, 171.